Detailed numerical analysis of the effect of radial column heterogeneities on peak parking experiments with slowly diffusing analytes

Huygens, Bram; Song, Huiying; Cabooter, Deirdre; Desmet, Gert

Published in:
Journal of Chromatography A

DOI:
10.1016/j.chroma.2021.462557

Publication date:
2021

Detailed numerical analysis of the effect of radial column heterogeneities on peak parking experiments with slowly diffusing analytes

Bram Huygens[(1)], Huiying Song[(2,3)], Deirdre Cabooter[(2)], Gert Desmet[(1,*)]

[(1)] Vrije Universiteit Brussel, Department of Chemical Engineering, Pleinlaan 2, 1050 Brussel, Belgium

[(2)] KU Leuven, Department for Pharmaceutical and Pharmacological Sciences, Pharmaceutical Analysis, Herestraat 49, Leuven, Belgium

[(3)] current affiliation: Janssen Pharmaceutica, Process Analytical Research, Chemical Process Research & Development, Turnhoutseweg 30, Beerse, Belgium

(*) corresponding author: tel.: (+) 32 (0)16.32.34.42, fax: (+) 32 (0)16.32.34.48, e-mail: gedesmet@vub.be

Abstract

The origin of the peak skewness that can be observed when applying the deconvolution method to isolate the diffusion process from the flow processes for peak parking experiments conducted under conditions of slow radial equilibration and strong trans-column velocity gradients was investigated. Numerical simulations were carried out for a variety of trans-column velocity profiles and a broad range of experimental conditions and system parameters were investigated. Results show that, under the aforementioned conditions, the traditionally employed variance subtraction method displays a consistent error which follows the dynamics of the diffusive relaxation during both the peak parking and the flow steps. It is also found that, under the same conditions, the peak deconvolution method is bound to produce deconvoluted "parking-only" peaks that are strongly asymmetric, despite the perfectly symmetric nature of the pure diffusion process marking this parking step. It is shown that this asymmetry is acquired during the flow step following the parking stop. During this step, parked and non-parked peaks are deformed in different ways, despite being subjected to the same trans-column velocity profile. This different deformation cannot be filtered away with the deconvolution or the variance subtraction method, hence introducing an error. Solutions to alleviate the peak skewness and the variance error consist of parking the peak close to the inlet or the outlet or exiting the parked peak through the column inlet (flow reversal method). Under the considered conditions, these approaches could reduce the error on the measured effective diffusion coefficient up to 87%. Carrying out the variance subtraction or the deconvolution process with a peak that has also been parked for a substantially long parking time instead of using a "no-parking" peak as is customary done, is another option to counter the effect.

Keywords: deconvolution ; effective diffusion coefficient; numerical simulation; peak parking; peak symmetry ; radial heterogenity

1. Introduction

Peak parking experiments [1-9] were introduced in the field of chromatography after a taxi ride discussion between Knox and Giddings [10] and have since then played a crucial role in the interpretation of the band broadening data measured on a chromatography column. The measurement produces a value for the effective diffusion coefficient D_{eff}. This is not only a direct measure for the longitudinal diffusion or B-term band broadening, but, via the use of the effective medium theory, also allows to determine the value of the intra-particle diffusion coefficient [11,12]. This not only determines the C_s-term contribution but also influences the eddy-dispersion term [13]. Peak parking experiments also play an important role in the flow reversal method established by Felinger to determine dispersion losses in column fittings [14,15].

In brief, the traditional peak parking experiment uses Einstein's law of diffusion to determine D_{eff} from the difference in spatial variance $\Delta\sigma^2$ between an experiment with and one without peak parking and the duration t_{pp} of the parking process [16]:

$$D_{eff} = \Delta\sigma^2/2.t_{PP} \qquad (1)$$

The spatial variance σ^2 in Eq. (1) is obtained by multiplying the time variance with the square of the velocity of the retained peak when flowing through the column [16].

The direct reason for the present study was our interest in the peak skewness that was observed during peak parking experiments conducted with analytes displaying a low effective diffusion in a reversed-phase particle packed column (see Fig. 1 for an example). This skewness compromises the use of the peak widths conventionally used to determine the peak's variance (e.g., peak width at half height, 4σ- or 5σ-width), as these assume a Gaussian peak shape. The alternative approach to calculate the peak's variance, i.e., via the second order central moment, is also encumbered by the skew of the peak as it is generally more difficult to find the correct starting and end point of the peak when it is tailing or fronting [17,18]. The obvious solution to attenuate the skewness problem, i.e., using longer parking times, is in many cases not practical either because of the unaffordable waiting times. In addition, the longer waiting times also increase the probability of baseline shifts which can have a detrimental effect on the accuracy of the method of moments [19]. One approach to deal with such skewed peaks is to model them with an exponentially modified Gaussian (EMG), describing the symmetrical part of the peak shape with the classic variance σ^2 and representing the skewness using a relaxation parameter τ [18]. However, there is no physical link between this model and the true physics of the process, nor is there a theoretical framework that can be used to interpret the value of the τ-parameter which nevertheless contains an important part of the information on the peak shape. Attempting to remove the undesired skewness of the peak, we also tested the so-called deconvolution method [20,21], deconvoluting the parked peak with the peak signal obtained when the parking time is either zero or very small (see Eqs. (9) and (10) further on for the deconvolution procedure). The idea behind this approach is that it would filter out the band broadening acquired by the peak while flowing through the column, leaving only the band broadening acquired during the actual parking period. Given this broadening is exclusively originating from the longitudinal molecular diffusion, which is a perfectly symmetrical process, it was expected the deconvoluted peak would have been perfectly symmetrical as well and hence much easier to quantify than the original skewed peak. However, as can be noted in Fig. 1, this was not the case, and the deconvoluted peak displayed a clear skew (cf. the difference with the best-fit Gaussian peak (dashed curve) in Fig. 1). The skew was even more pronounced than the skew of the original non-deconvoluted parked and non-parked peaks shown in Fig. S-1 of the Supporting Material (SM).

The hypothesis underlying the present study is that the observed skewness originates from radial trans-column velocity gradients, in turn induced by radial gradients in packing density and the wall effect [22,23]. We surmise this because the theory used to interpret peak parking experiments (the variance method as well as the deconvolution method) is based on a 1-dimensional representation of the diffusion process, ignoring the existence of any radial concentration gradients. In case of slowly diffusing molecules and significant radial packing quality and density gradients, the trans-column velocity profile induced by the latter can be expected to give rise to significant radial concentration gradients, whose presence can be suspected to invalidate the 1D-simplification.

To investigate this hypothesis, a detailed view on the formation of the peak shape during the different steps of the peak parking process is needed. The investigation is therefore carried out numerically, studying the time-dependent solution of the complete advection-diffusion mass balance in cylindrical coordinates:

$$\frac{\partial C}{\partial t} = -u(r)\frac{\partial C}{\partial x} + D_{ax}\frac{\partial^2 C}{\partial x^2} + D_{rad}\left(\frac{\partial^2 C}{\partial r^2} + \frac{1}{r}\frac{\partial C}{\partial r}\right) \tag{2}$$

where $u(r)$ is the velocity, which varies across the column's cross-section, and D_{ax} and D_{rad} are the axial and radial dispersion coefficients, respectively. As specified in Section 2.2, these parameters were chosen to lump the properties of both the mobile and stationary phase, thus including their dependence on retention. Note that the original 3D cylindrical column geometry is reduced here to a 2D geometry because of the assumed angular symmetry, a common simplification for packed bed columns [22].

A broad variety of different trans-column velocity profiles is considered. In the main text, all results relate to either a pure parabolic profile or a profile taken from literature [23,24] and commonly accepted as a realistic profile for the side-wall region of state-of-the-art packed bed columns (referred to as “side-wall“). In the SM, however, a panoply of other shapes is considered. For the sake of simplicity, it is assumed the profiles remain unchanged along the column axis. Please note the considered velocity profiles only represent a relatively small deviation from the plug flow character of the flow (e.g., the parabolic flow profile in Fig. 2a does not tend to a zero velocity near the walls as is the case in Poiseuille flow through an open tube but tends to a velocity that is only a few % smaller than in the center).

2. Numerical and experimental methods

2.1 Experimental methods for peak parking experiments

Peak parking experiments were performed on an Ultimate 3000 HPLC system from Dionex (now Thermo Scientific, Germering, Germany) equipped with a high-pressure pump, an autosampler and UV/VIS variable wavelength detector with a flow cell of 11 µL. The overall system volume was 20 µL. The sampling rate was set at 40 Hz. Chromeleon software (Thermo Scientific) was used for data acquisition and instrument control. The injection volume was 1 µL and the column temperature was kept constant at 30°C using a Spark Mistral oven (Emmen, Netherlands). The detection wavelength was set at 254 nm. HPLC grade acetonitrile (ACN) was obtained from Fisher Chemicals (Merelbeke, Belgium). Milli-Q water was prepared in the lab using a Milli-Q gradient water purification system from Millipore (Bedford, MA, USA). Caffeine was from Sigma-Aldrich (Diegem, Belgium). A Zorbax Stable Bond C_{18} column (4.6 × 100 mm, 3.5µm) was obtained from Agilent Technologies (Diegem, Belgium). A stock solution of caffeine was prepared in Milli-Q water in a concentration of 10.000 ppm and refrigerated. Fresh samples with a concentration of 1000 ppm were prepared daily in the mobile phase. The mobile phase consisted of ACN/H_2O (5/95, v/v). Caffeine was injected into the column at a flow rate of 0.5 mL/min. When the compound reached the middle of the column, the flow was stopped for 150 min. Afterwards, the flow was resumed and the analyte peak eluted from the column towards the detector.

2.2 Numerical methods for peak parking simulations

Peak parking experiments were simulated by solving the time-dependent advection-diffusion problem in cylindrical coordinates, as given by Eq. (2). This was done by means of an in-house written MATLAB® code, implementing an implicit finite element method [25], with a grid spacing of $10\ \mu m$ and a time step of $50\ ms$.

Since the subject of this study is the effect of radial heterogenities on the trans-column level, the concentration profiles were not resolved on the level of individual pores and particles. Instead, the parameters of Eq. (2) were chosen to lump the properties of both the mobile and stationary phase, such that the advection term was written in terms of the retained velocity ($u = u_0/(1+k)$, where u_0 is the unretained velocity and k is the retention factor) and the diffusion terms were written in terms of the effective dispersion coefficients (which depend on the retention factor as well), both axial and radial. Furthermore, for the sake of computational efficiency, the peak's center of mass was kept at the center of the computational domain ($x = 0$) by subtracting the mean velocity from the velocity fields given below.

In the case of the parabolic flow profile, the velocity is given by (see Fig. 2a):

$$u(r) = \frac{u_0}{1+k}\left(1 - \omega\frac{r^2}{r_c}\right) \quad (3)$$

Where ω is the relative velocity difference (ω=Δu/u) between axis and wall, and r_C is the column radius.

In the case of the side-wall flow profile, the velocity is given by (see Fig. 2b):

$$u(r) = \frac{u_0}{1+k}\left(1 + \omega_{TLOPL}\cdot\exp\left(\frac{r-r_c}{d_p}\right) - \omega_{WDRPL}\cdot\exp\left(\frac{r-r_c}{6d_p}\right)\right) \quad (4)$$

Where ω_{TLOPL} and ω_{WDRPL}, respectively, are the relative velocity differences resulting from the 'thin and loose orderly packed layer' and the 'wide and dense randomly packed layer', as described in [23] and [24], and d_p is the particle diameter. With $\omega_{TLOPL} = 1.50$ and $\omega_{WDRPL} = 0.50$, this flow profile has a 'velocity well' of $\Delta u/u = 0.23$ (see Fig. 2b).

In addition, a simulation was done with a plug flow profile ($u = u_0/(1+k)$ for all r), to validate the accuracy of the performed simulations.

An overview of the simulation parameters is given in Table 1. Unless otherwise specified, the parameter values given here apply to all results discussed in Section 3. Note that during the peak parking regime of the simulations, u_0 was set to zero and D_{ax} and D_{rad} were both set to D_{eff} (as diffusion is the only source of dispersion under these conditions).

2.3 Data analysis and deconvolution

At each time step of the simulations, the concentration profile's zeroth, first, second and third order moment (M_0, M_1, M_2 and M_3) were computed, from which the peak's variance (σ^2) and skewness (γ) were subsequently derived (note that the peak's center of mass was kept at $x = 0$):

$$M_n = \iiint_V x^n C \cdot dV = \iint_V x^n C \cdot 2\pi r dr dx \tag{5}$$

$$\sigma^2 = \frac{M_2}{M_0} \tag{6}$$

$$\gamma = \frac{M_3/M_0}{\sigma^3} \tag{7}$$

Furthermore, the concentration profile was recorded at three steps: at the beginning of the peak parking, at the end of the peak parking and as the peak exited the column. From this data, the peak shape was computed by integrating over the column's cross-section:

$$f(x) = \iint_S C(x,r) \cdot dS = \int_S C(x,r) \cdot 2\pi r dr \tag{8}$$

The peaks resulting from simulations with ($f_{with\ PP}$) and without ($f_{without\ PP}$, see further on) peak parking were then deconvoluted in MATLAB®, using the fft (Fast Fourier Transform) and $ifft$ (Inverse Fast Fourier Transform) functions, analogous to the method described in [21].

Firstly, the Fourier transform F(ξ) of both peaks was computed:

$$F(\xi) = \int_{-\infty}^{+\infty} f(x) e^{-i\xi x} \cdot dx \tag{9}$$

Secondly, the two computed spectra were divided, and the deconvoluted curve in the space domain f(x) was computed as the inverse Fourier transform of the resulting spectrum:

$$f_{PP}(x) = \frac{1}{2\pi} \int_{-\infty}^{+\infty} \frac{F_{with\ PP}(\xi)}{F_{without\ PP}(\xi)} e^{i\xi x} \cdot d\xi \tag{10}$$

As both $F_{with\ PP}$ and $F_{without\ PP}$ tend to zero as the wavenumber (ξ) tends to infinity, the division in Eq. (10) is error-prone, leading to spurious oscillations in the resulting deconvolution. Therefore, the deconvolution method involves a curation step, in which the spectrum values above a chosen cut-off wavenumber (ξ_{CO}) are discarded. Note that this computational issue is less pronounced in numerical results than it is in experimental results, because of the lack of noise affecting the spectra.

3. Results and discussion

Before proceeding, it is important to note that the examples shown here relate to cases of very strong axial and/or very slow radial dispersion, i.e., for cases where the time needed for the axial flow process is much shorter than the time needed for radial equilibration. From the Taylor-Aris dispersion theory

[26], the time constant in the exponential of the slowest converging term (which could be used as proxy for the characteristic time for radial equilibration) is known to be given by (see also discussion of Eq. (20) further on):

$$\tau_{rad} = \frac{1}{58.7}\frac{d_c^2}{D_{rad}} \tag{11}$$

Thus, considering the parameter values given in Table 1, the residence time in the absence of peak parking ($t_R = 10\ min$) is clearly insufficient for radial equilibration ($\tau_{rad} = 23\ min$). This is a case that in practice can be expected to occur in case of poorly packed columns displaying a strong trans-column velocity profile and slowly diffusing molecules.

3.1 Example and general problem description

Fig. 3 and 4 show the concentration contour plots and their corresponding radially averaged concentration profile for the parabolic (Fig. 3) and the side-wall profile (Fig. 4) at three different moments in time: just before and just after the peak parking process (resp. panels a,e and panels b,f) and at the end of the column (panels c,g). The initial peak (column inlet) was in all cases a perfectly rectangular band with a width of 20 μm and peak parking was carried out exactly halfway the column. For the sake of comparison, the profiles obtained at the end of the column in the absence of peak parking are given in panels d,h.

As can be noted from panels a,e, the bands are under the presently considered conditions significantly warped when arriving at the parking position and then axially and radially spread into a perfectly rectangular shape by the end of the parking period (panels b,f). The band subsequently warps again during the subsequent flow trajectory towards the column end (panels c,g), during which it deforms according to the prevailing trans-column velocity profile.

As is customarily done, the information about the shape of the concentration distributions shown in Figs. 3-4 has been quantified (and condensed) via their variance (σ^2) and skewness (γ). These are shown in Fig. 5 as a function of the time for the case with and without peak parking. Please note that the dashed part of the curve shown for the “no-parking”-case does not represent any physical process, but just reflects a jump in time added to have the BC-trajectories directly underneath each other to facilitate their comparison (the true time coordinate for the BC-trajectory in the “no parking”-case is hence equal to the time on the x-axis minus the duration of the peak parking in the case with peak parking).

Fig. 5a and 5d show that, as expected, the increase of the variance with time in the first flow part (AB trajectory) is the same for the cases with and without peak parking. An important difference can, however, be noticed in the second flow part (BC trajectory), where the increase of the band's variance with time is clearly less steep after an intermediate peak parking step than it is in the "no parking"-case (cf. the zoom of Fig. 5a in Fig. 5b). In the latter case, the evolution of σ^2 with time during the BC-trajectory is the mere continuation of the (ever-steepening) relation between variance and time already marking the AB-trajectory. This ever-steepening trend is a direct reflection of the fact that, for time scales shorter than τ_{rad} (cf. Eq. (11)), σ^2 is known to vary with a power >1 (initially this power is even exactly = 2 [27]). In the case with peak parking, the band broadening process during the BC-trajectory restarts from a radially uniform band (at least when the parking time is several times larger than τ_{rad}), as is the case in the AB-trajectory. Since the σ^2-evolution is fully determined by the shape of the band at the onset of the dispersion process [26], σ^2 can hence be expected to follow exactly the same trend as in the AB-trajectory. The relation between σ^2 and time is less steep than in the later stages marking the BC-trajectory of the no-parking case, hence explaining why the σ^2-evolution is steeper in the no-parking case than in the case with peak parking.

The fact that the growth in variance during the AB-trajectory is the same with and without peak parking, while it is clearly larger in the subsequent BC-trajectory in the no-parking case automatically implies that the variance gained during the uninterrupted flow trajectory AC as experienced in the no-parking case is not equal to but larger than the sum of the variances of the two flow processes AB and AC. Mathematically, this can be expressed as follows ($\Delta\sigma^2$ is the variance in space coordinates):

$$\Delta\sigma^2_{\text{AC,no parking}} > \Delta\sigma^2_{\text{AB}} + \Delta\sigma^2_{\text{BC,with parking}} \qquad (12)$$

Eq. (12) reflects the well-established fact that the variances of successive individual dispersion processes are only strictly additive when these are independent of each other [28]. Flow systems displaying a radial velocity gradient and a slow radial equilibration are a classic example where this independency is not respected [29]. In the "no parking" experiment, molecules that were either residing in a slow or a fast-moving region in the AB-trajectory will under the presently considered conditions to a very large extent also still do so in the BC-trajectory. In other words, the dispersion history they experience in the two subsequent processes is not independent. In the run with peak parking stop, analytes starting their BC-trajectory have the opportunity to completely "forget" their flow history in the AB-trajectory provided the stop lasts long enough to achieve complete radial equilibration, such that in this case the additivity assumption is valid (cf. Eq. (13a) further on).

Further introducing $\Delta\sigma^2_{\mathrm{tot,with\ PP}}$ and $\Delta\sigma^2_{\mathrm{tot,no\ PP}}$ as the variances measured at the end of the column respectively with and without peak parking, and $\Delta\sigma^2_{\mathrm{PP}}$ as the true variance acquired during the parking process, we can write:

$$\Delta\sigma^2_{\mathrm{tot,with\ PP}} = \Delta\sigma^2_{\mathrm{AB}} + \Delta\sigma^2_{\mathrm{PP}} + \Delta\sigma^2_{\mathrm{BC}} \tag{13a}$$

$$\Delta\sigma^2_{\mathrm{tot,no\ PP}} = \Delta\sigma^2_{\mathrm{AC,no\ PP}} \tag{13b}$$

With Eq. (12), it is then straightforward to note:

$$\Delta\sigma^2_{\mathrm{PP,measured}} = \Delta\sigma^2_{\mathrm{tot,with\ PP}} - \Delta\sigma^2_{\mathrm{tot,no\ PP}} < \Delta\sigma^2_{\mathrm{PP}} \tag{14}$$

In other words, the fact that the increase in variance during the BC-trajectory in general depends on the band variance and band shape acquired during the preceding processes invalidates the classic approach adopted to determine $\Delta\sigma^2_{\mathrm{PP}}$ from the difference in variance between a run with and without peak parking in cases where the flow process leads to a strong radial warp of the band shape, as is the case in the present example.

Turning now to the skewness of the band, it can be verified from Figs. 3 and 4 that the skewness acquired by the peak during the BC trajectory is clearly smaller than that acquired during the AB trajectory (compare skewness between panels e and g) despite the flow process underlying this skewing is the same. This is essentially caused by the fact that the peak width and shape during the BC-trajectory is for a large part determined by the (symmetrical) broadening acquired during the parking process, such that the (asymmetrical) broadening originating from the flow process has a relatively smaller impact on the band shape than it did in the AB-trajectory, which started from a much narrower and consequently more easily deformable band.

The above can be assessed in a more quantitative form from the plots of the evolution of the band's skewness (γ) with time as represented in Figs. 5c and 5f. Please note that the side-wall and the parabolic flow profiles lead to a different sign of γ, resp. displaying a negative and a positive skew. In the side-wall profile case, the most significant deviation from the mean velocity is the tailing velocity near the wall. As the fronting part immediately next to the wall is too small to counter this effect, it is indeed obvious to observe a tailing band (and hence a negative skew). In case of the parabolic flow profile, the incurred skewness is substantially smaller than in case of the side-wall flow profile. This seems to be related to the much more gradual variation of the radial velocity profile.

Considering now first the runs with peak parking, it is in both cases observed that the skewness of the band at the end of the BC-trajectory is much smaller than that incurred during the AB-trajectory, as a direct consequence of the band straightening effect of the peak parking process. In agreement with physical expectations, we also see the skewness at the end of the “no-parking” runs is much higher (=further away from zero) than the skewness of the bands subjected to an intermediate parking stop, as an obvious consequence of the fact that the former did not undergo the radial equilibration effect of the peak parking process.

3.2 Deconvolution method

Addressing now the use of the deconvolution process as a potential solution to remove the skewing effect of the flow trajectories AB and BC, the black curves in Fig. 6a,b show the band shapes obtained by deconvoluting a band recorded at the column’s end after a parking stop with a “no parking” band. As can be noted, the deconvoluted band deviates from the perfect Gaussian shape (gray curves) expected based on the perfectly symmetrical nature of the diffusion-only band broadening process experienced during the parking stop. For the side-wall flow profile, the deviation is relatively small, although the presence of a part with negative values of the deconvolution curve is certainly disturbing. Especially not given the high accuracy of the numerical simulations, implying the negative part of the curve cannot be considered as a measurement artefact. The latter can be appreciated from Fig. S-2, where a similar exercise is made for the case of a pure plug flow transcolumn velocity profile. As can be noted, the resulting deconvoluted curve representing the “parking only” band broadening is perfectly Gaussian in this case, without any negative values on the curve. For the parabolic flow profile, the deconvoluted peak can even be categorized as strongly non-Gaussian, given the strong pattern of wiggles at its right-hand side. The observed asymmetries are also no numeric artefacts, as can be witnessed from the perfectly symmetrical gray curves in Fig. 6a-b. These are obtained by deconvoluting the band obtained immediately after the parking process (panels c,f in Fig. 3-4) with the band just prior to the parking process (panels b,e in Fig. 3-4). Please note that this deconvolution exercise is not possible in practice, as the required information about the in-column band shape is not available to the experimenter. This impediment is not present in the current simulation study, allowing us to show the deconvolution process is indeed capable of isolating and hence demonstrating the pure symmetric nature of the diffusion process, despite the strongly asymmetric shape of the input profiles (see e.g., Fig. 4h). However, this is only possible if no other, dependent processes are involved.

Mathematically, this can be understood as follows. Adopting the $*$-notation for the convolution operator [29], the functions describing the peak observed at the end of a run with peak parking and one without peak parking can respectively be written as:

$$f_{with\ parking} = f_{AB} * f_{PP} * f_{BC,with\ parking} \quad (15a)$$

$$f_{no\ parking} = f_{AC,no\ parking} = f_{AB} * f_{BC,no\ parking} \quad (15b)$$

wherein the individual f's on the right-hand side of the equations represent the different band broadening processes experienced by the band during the AB-, BC- or AC-trajectories or during the peak parking events.

Next, it is a well-established fact that the shape of a band undergoing a deformation by a laminar flow process will remain to depend on its initial shape as long as the radial concentration gradients are not completely wiped out by radial equilibration, as already remarked when explaining the different σ_{BC}^2-trajectories in Figs. 5a,d. Considering then that the BC-trajectory in the case with peak parking starts from a perfectly rectangular and radially homogenized band (panels b,f in Fig. 3-4) while the BC-trajectory in the case without peak parking starts from the warped band marking the end of the AB-trajectory (panels a,e in Fig. 3-4), it readily follows that the peak transformations $f_{BC,with\ parking}$ and $f_{BC,no\ parking}$ will be different:

$$f_{BC,with\ parking} \neq f_{BC,no\ parking} \quad (16)$$

Subsequently switching to the Fourier-domain, where the deconvolution process reduces to a mere division (see Eqs. (9) and (10)):

$$F_{PP,measured}(\xi) = \frac{F_{with\ parking}(\xi)}{F_{no\ parking}(\xi)} = \frac{F_{AB}(\xi).F_{PP}(\xi).F_{BC,with\ parking}(\xi)}{F_{AB}(\xi).F_{BC,no\ parking}(\xi)} \neq F_{PP}(\xi) \quad (17)$$

it can easily be understood that the deconvoluted parking peak ($f_{PP,measured}$-peak, obtained by back-transforming $F_{PP,measured}$ via Eq. (10)) will not reflect the true (symmetrical) diffusion process, as the division on the right hand side of Eq. (17) will not entirely remove the F_{BC}-factors. Note that the capital F in Eq. (17) represents the Fourier-transforms of the corresponding lower-case f in Eq. (15).

When deconvoluting the profiles in the b-panels of Figs. 3-4 with those in the a-panels (which is the process leading to the perfectly Gaussian gray curves in Fig. 6), the F_{BC}-factor is not present, and in this case the deconvoluted signal exactly reflects the diffusion-only process:

$$F_{PP,measured}(\xi) = \frac{F_{after\ parking}(\xi)}{F_{before\ parking}(\xi)} = \frac{F_{AB}(\xi).F_{PP}(\xi)}{F_{AB}(\xi)} = F_{PP}(\xi) \quad (18)$$

With the above, it can be ascertained that the asymmetry of the deconvoluted peaks represented by the black curves in Fig. 6 arises from the difference in band deformation after the parking process, and not from any asymmetry created during the peak parking process itself. Despite the strong radial warp of the peak at the start of the peak parking, the radial concentration gradients marking its shape clearly do not lead to any distortion of the axial diffusion process, which proceeds in a perfectly symmetrical and Gaussian manner (cf. the gray curves in Fig. 6).

Admittedly, none of the black curves in Fig. 6 is a close fit to the experimentally observed $f_{PP,measured}$-peak shown in Fig. 1 and lying at the origin of the present study. However, the huge diversity in the deformation patterns observed in Figs. S-3 and S-4 of the SM for a broad variety of other transcolumn velocity profiles shows how sensitive the deconvoluted curve is to the exact shape of the radial velocity distribution. A good agreement between simulation and experiment will hence only be possible provided the simulation exactly uses the true radial velocity profile. In practice, however, the latter is unknown such that a good agreement can only be obtained by “guessing” the right profile (and hoping the radial velocity profile remains more or less constant along the axis, for this would add another variable to the problem). In fact, one could think of using the agreement (if found) to infer the actual radial velocity profile.

Please note when comparing Fig. 1 with the profiles in Fig. 6, that the latter plots are plotted in the x-domain such that the front and tail end of the peak are switched. In the SM, the bands shown in Fig. 6 are represented in the time domain (cf. fig. S-5 of the SM).

The degree of distortion to which the deconvoluted $f_{PP,measured}$-peak is subjected can be expected to be directly linked to the degree of deformation the peak undergoes during the flow trajectories. This is illustrated in Figs. 7a,c, showing the $f_{PP,measured}$-peak is more strongly distorted when the radial velocity gradient increases in strength. In case of the parabolic flow profile, the deformation effect is very pronounced, cf. the huge wiggles appearing on the peak’s right-hand side.

From the discussion of Figs. 5 and 6, the degree of distortion of the $f_{PP,measured}$-peak can also be expected to depend on the peak parking time. This is illustrated in Figs. 7b,d. The blue curves represent a case where the peak parking time is considerably larger than in the reference case in Fig. 6. In this case, the distortive part of the devonvolution (cf. division of $F_{BC,with\ parking}$ and $F_{BC,no\ parking}$ in Eq. (17)) is ‘overshadowed’ or ‘smoothened’ by the diffusive part of the deconvolution (cf. F_{PP} in Eq. (17)), resulting in a peak that appears Gaussian.

When the peak parking time is considerably shorter (red curves), the resulting $f_{PP,measured}$-peak could be expected to be relatively undistorted as well, because of the smaller difference between $F_{BC,with\,parking}$ and $F_{BC,no\,parking}$. However, since there has been less axial diffusion (F_{PP}) to overshadow or smoothen the distortion, the peak appears especially distorted instead. Furthermore, when parking times are extremely short, a regime is hit wherein the deconvolution method has to reconstitute a peak that is extremely narrow (as a reflection of the small degree of extra band broadening the peak parking process has caused). The back-transformation of such narrow peaks is known to be plagued by the Gibbs-phenomenon [20], which arises from the need to filter the Fourier spectrum by means of a cut-off wavenumber. The Gibbs-phenomenon also introduces a pattern of wiggles, which, however, should not be confused with the wiggles caused by the deformation caused by a parabolic flow profile. Unlike the latter, which clearly only appear on one side of the peak, the Gibbs-wiggles are more symmetrical. Both phenomena can hence be relatively easily distinguished (e.g., the wiggles appearing in Fig. 7d are clearly related to the Gibbs phenomenon, as they appear in equal amounts on both sides of the band). A thorough discussion of the conditions under which the Gibbs-wiggles appear during peak deconvolution is given in [21]. The difference in peak width between the peaks with and without parking in the case leading to the red curves in Figs. 7b,d falls within the criterion established in that study, hence explaining the occurrence of the Gibbs-wiggles.

The distinction between the Gibbs phenomenon and the effect of the flow profile rules out that this effect is a result of filtering the Fourier spectrum. This is further supported by Fig. S-6 of the SM, demonstrating the choice of a suitable cut-off wavenumber.

3.3 Variance substraction method

Leaving now the peak deconvolution technique for the more customary practice of variance subtraction, the aforementioned effect of parking time and magnitude and shape of the radial velocity gradient are quantified and expressed in Fig. 8 as the difference between the true variance of the parking-only process ($\Delta\sigma^2_{\mathrm{PP}}$) and the actually measured one (via Eq. (6)):

$$\Delta\sigma^2_{PP,error} = \Delta\sigma^2_{PP} - \Delta\sigma^2_{PP,measured} = 2D_{eff}t_{PP} - \Delta\sigma^2_{PP,measured} \tag{19}$$

As can be noted, the $\Delta\sigma^2_{\mathrm{PP,error}}$-values as defined in Eq. (19) are consistently positive, in full agreement with the < sign in Eq. (14). Physically, this implies that when the band experiences a radial velocity profile during its progress through the column, the concomitant peak parking experiment can be expected to lead to an underestimation of the true peak parking variance, and hence also of the true effective diffusion coefficient (D_{eff}), because the subtraction in Eq. (14) overestimates the band broadening incurred during the BC-trajectory of a parked peak. In most practical cases the underestimation of D_{eff} is insignificant, but this is no longer true in cases of large transcolumn velocity gradients and slow radial equilibration such as those considered here.

In agreement with physical expectations, Figs. 8a,c show how $\Delta\sigma^2_{\mathrm{PP,error}}$ grows with increasing radial velocity difference in the presently considered case of slow radial equilibration. The parabolic profile clearly increases much more rapidly with $\Delta u/u$ than the side-wall profile (cf. the difference in scale of the x-axis of Fig. 8a and 8c), in full agreement with the fact that the latter is in essence much flatter than the parabolic profile. In both cases, the relation between $\Delta\sigma^2_{\mathrm{PP,error}}$ and $\Delta u/u$ was found to be quadratic, in agreement with the Taylor-Aris dispersion theory [26].

The error obviously also grows with increasing parking time because, the larger this time, the more strongly the radial deformation experienced in the AB-trajectory will be countered. For very large parking times, this effect however levels off because in this regime the radial equilibration of the band is complete, in which case the difference in variance gained during the BC-trajectory has reached its maximum. Note that although the absolute error on $\Delta\sigma^2_{PP}$ increases with the peak parking time, the relative error actually decreases, because $\Delta\sigma^2_{PP}$ itself increases linearly. This result agrees with the discussion of Figs. 7b and 7d, where the deconvolution's distortion becomes less significant as the peak parking time increases.

Since the $\Delta\sigma^2_{\mathrm{PP,error}}$-value is directly linked to the radial diffusive equilibration, it is evident to see its dependency on the parking time exactly follows the dynamics of the radial diffusion process. Solving the transient radial diffusion equation, it can be shown the degree of radial equilibration can generally be written as a summation of exponential decay functions [26]:

$$\Delta\sigma^2_{PP,error} = \sum_{n=1}^{\infty} \alpha_n (1 - \exp(-\beta_n t_{PP})) \tag{20}$$

wherein β_n (with n=1,2,…) is the proportionality constant in the exponential decay function describing the radial diffusive relaxation process in the n^{th}-term of the summation and wherein α_n is the amplitude of the same term. According to theory, α_n is related to the deformation of the band during the AB- and BC-trajectories, and $\beta_n = 4j_{1,n}^2 \cdot D_{rad}/d_c^2$, where $j_{1,n}$ is the nth zero of the Bessel function J_1. In particular, the first (and 'slowest') term of Eq. (20), for which $\beta_1 = 58.7 \cdot D_{rad}/d_c^2$, can be considered as a good proxy for the characteristic time for radial equilibration (cf. Eq. 11).

Depending on the shape of the velocity field, this series either converges very rapidly (1st term is dominant), as is the case for the parabolic profile, or very slowly, as is the case for the side-wall profile. In the latter case, the need to involve a large number of terms gravely complicates the determination of the α_n-values by numerical fitting as in the present study. To circumvent this fitting problem, the fitting as shown in Figs. 8b,d was limited to only three terms. In the parabolic case, it was found that $\alpha_1 \gg \alpha_2, \alpha_3$, whereas α_2 and α_3 were of a more significant nature in the side-wall profile case.

In case of the parabolic velocity field, where the velocity gradient spans the entire column cross-section, the first term is clearly dominating, such that the evolution of $\Delta\sigma^2_{\mathrm{PP,error}}$ can be represented with a good degree of accuracy by the simpler:

$$\Delta\sigma^2_{PP,error} = \alpha(1 - \exp(-\beta t_{PP})) \tag{21}$$

Fitting Eq. (21) to the numerical data in Fig. 8b, the fitted β-value ($\beta = 64.3 \cdot D_{rad}/d_c^2$, $R^2 = 0.9998$) differs slightly from the theoretically expected value of $\beta_1 = 58.7 \cdot D_{rad}/d_c^2$. This difference is most probably due to the interference from the higher order terms, which are small but not zero.

Likewise, the α-value could be determined by fitting Eq. (21) to the numerical data in Fig. 8b. By repeating this for various values of all relevant parameters, α could be modelled as a function thereof. Apart from the $\alpha \sim \Delta u^2$ dependency shown in Fig. 8a, α was found to depend on the radial dispersion (cf. dependency on D_{rad} and d_c^2), but the characteristic time here is linked to the duration (t_{AB}, t_{BC}) of the two flow processes instead of the duration of the parking process. Based on the fitted α-values, the following expression was obtained:

$$\alpha = \frac{1}{6}\Delta u^2 t_{AB} t_{BC} \exp\left(-58.7\frac{D_{rad}}{d_c^2}\sqrt{t_{AB} t_{BC}}\right),\ \ with\ \Delta u = \omega\frac{u_0}{1+k} \tag{22}$$

Given the physical meaning of α_1 (=dependent on the initial band shape), the dependency on $t_{AB}.t_{BC}$ makes perfect sense since these are the parameters controlling the degree of peak deformation (band warp) and hence also the shape of the band at the start of the different steps in the peak parking process. The fact that $t_{AB}.t_{BC}$ appears as their product indicates the duration of the AB-trajectory and the

BC-trajectory have a similar impact on this process. Or at least, it indicates that, when either one of them turns to zero, the error turns to zero as well.

3.4 Possible solutions to minimize the effect

The fact that t_{AB} and t_{BC} only appear as their product also implies that, since t_{AB} + t_{BC} =fixed, the error on $\Delta\sigma^2_{\mathrm{PP,measured}}$ is largest when t_{AB} = t_{BC}, i.e., when the peak is parked in the middle of the column. And it would be minimal if either t_{AB} or t_{BC} would be minimal, i.e., when the peak would either be parked very close to the inlet or very close to the outlet. This is verified in Figs. 9a,c (red curves), showing the effect by means of the deconvoluted peaks. The curves for parking at the inlet vs parking at the outlet overlap perfectly, thus reflecting the interchangeability of t_{AB} and t_{BC} in Eq. (g4). The overlap is perfect in case of both considered flow profiles. The deconvoluted peaks are also significantly less distorted than in the mid-column parking case. For the examples under consideration, $\Delta\sigma^2_{\mathrm{PP,error}}$ values drop from $0.495\ mm^2$ to $0.276\ mm^2$ in the case of the parabolic flow profile and from $0.483\ mm^2$ to $0.284\ mm^2$ in the case of the side-wall flow profile.

Inspired by the recent flow reversal work of Felinger and Gritti [15,30], a close inspection of Eq. (22) also suggests an even more powerful approach to reduce the error on $\Delta\sigma^2_{\mathrm{PP,measured}}$, i.e., by making both t_{AB} and t_{BC} as small as possible. In practice, this involves parking the band close to the inlet, and then reversing the flow such that the band exits again along the nearest exit (which originally was the column inlet). The blue curves in Figs. 9a,c indeed confirm this ($\Delta\sigma^2_{\mathrm{PP,error}}$-values now drop to $0.065\ mm^2$ in the case of the parabolic flow profile and to $0.100\ mm^2$ in the case of the side-wall flow profile). As a side note, this approach also causes the sign of the error to change, thus slightly overestimating instead of underestimating the effective diffusion coefficient.

Considering that the root cause of the error on $\Delta\sigma^2_{\mathrm{PP,measured}}$ is a difference in band deformation experienced after the parking process, another way to reduce this difference, and hence $\sigma^2_{\mathrm{PP,error}}$, consists of replacing the "no parking" concentration profile that is normally used to eliminate the effect of the flow trajectories by one that has also already experienced a substantial parking time. This is illustrated in Figs. 9b,d, showing that the deconvoluted peak obtained when deconvoluting a peak with a parking time of 160 min with one obtained after a parking time of 80 min is clearly much more symmetrical than the peak obtained after deconvoluting a peak with a parking time of 80 min with one obtained after a zero parking time experiment ($\Delta\sigma^2_{\mathrm{PP,error}}$ values drop from $0.495\ mm^2$ to $0.014\ mm^2$ in the case of the parabolic flow profile and from $0.483\ mm^2$ to $0.007\ mm^2$ in the case of the side-wall flow profile). In the terminology used in Eq. (17), this can be understood by noting that deconvoluting the parking peak with another parking peak (one relating to a shorter parking time), the difference between the two F_{BC}-values that in that case appear in the division in Eq. (17) will be smaller than when deconvoluting the parking peak with a “no-parking” peak as is customarily done. When determining D_{eff} via linear regression of a ($\Delta\sigma^2$,t_{PP})-plot, the customary approach in literature [1-9], this approach can be mimicked by only fitting those data points with a sufficiently long peak parking time (i.e., several times τ_{rad}) and discarding the others.

4. Conclusions

Peak parking experiments carried out with slowly diffusing analytes ($\tau_{rad} > t_R$) in columns displaying a strong trans-column velocity profile (e.g., parabolic flow profile with $\Delta u/u > 0.02$ or side-wall flow profile with $\Delta u/u > 0.10$) can lead to an inherent error on the determined D_{eff}-value when using the variance subtraction method, or, equivalently, lead to skewed parking-only peaks when using the deconvolution method. I.e., the intrinsically perfectly symmetrical diffusion process marking the parking-only step nevertheless leads to an asymmetrical deconvoluted “parking-only”-peak. Depending on the exact shape of the trans-column velocity profiles, this skewness can be accompanied by strong oscillations (comprising strongly negative “concentration” values) marking one side of the peak. These oscillations differ from the more familiar Gibbs phenomenon (which only occurs when the difference in peak width between the parked and the non-parked peak becomes too small).

The D_{eff}-error and the skewness and oscillations marking the “parking-only”-peak are caused by the fact that the distortion of the band incurred after the parking stop is not the same as incurred along the same trajectory, but without preceding parking stop. Consequently, the “no parking” peak cannot be used to perfectly filter away the flow dispersion effects on the parked peak case, thus leading to an overcorrection and hence distortion of the (intrinsically Gaussian) “parking-only”-peak. The difference in band deformation during the post-parking trajectory is in turn due to the fact that, under conditions of slow radial equilibration, the evolution of a band’s shape strongly depends on its initial shape. And the initial shape at the start of the post-parking trajectory differs strongly between a parking and a no-parking case. In the former it has a rectangular, radially uniform shape as acquired during the long parking period, while in the latter is has the strongly warped shape with which it ended the pre-parking trajectory.

The exact skewness and shape of the deconvoluted “parking-only”-peak depends strongly on the exact shape of the trans-column velocity profile, making it very difficult to exactly model the effect because this profile is unknown and might also vary along the column axis.

The error and skewness grow with increasing radial velocity difference, with increasing length of the pre- and post-parking distances as well as with increasing parking time (although this trend levels off to a quasi-constant value such that the relative error on D_{eff} decreases). The two last observations can be used to suggest a number of solutions to alleviate the problem. These involve parking the peak either close to the inlet or the outlet or, even better, parking it close to the inlet and exiting it through the same column inlet using the flow reversal method, at least provided the D_{eff}-measured at these locations can be considered representative for the rest of the bed. It is known from literature Replacing the “no-parking” peak by a parked peak collected after a substantially long parking time is another option to counter the effect.

References

[1] J.H. Knox, H.P. Scott, B and C terms in the Van Deemter equation for liquid chromatography, J. Chromatogr. A 282 (1983) 297–313, http://dx.doi.org/10.1016/S0021-9673(00)91609-1.

[2] F. Gritti, G. Guiochon, Effect of the surface coverage of C18 -bonded silica particles on the obstructive factor and intraparticle diffusion mechanism, Chem. Eng. Sci. 61 (2006) 7636–7650, http://dx.doi.org/10.1016/j.ces.2006.08.070

[3] K. Miyabe, Y. Matsumoto, G. Guiochon, Peak parking-moment analysis. A strategy for the study of the mass-transfer kinetics in the stationary phase, Anal. Chem. 79 (2007) 1970–1982, http://dx.doi.org/10.1021/ac061321h.

[4] G. Desmet, K. Broeckhoven, J. De Smet, S. Deridder, G.V. Baron, P. Gzil, Errors involved in the existing B-term expressions for the longitudinal diffusion in fully porous chromatographic media. Part I: computational data in orderedpillar arrays and effective medium theory, J. Chromatogr. A 1188 (2008) 171–188, http://dx.doi.org/10.1016/j.chroma.2008.02.018.

[5] A. Liekens, J. Denayer, G. Desmet, Experimental investigation of the difference in B-term dominated band broadening between fully porous and porous-shell particles for liquid chromatography using the effective medium theory, J. Chromatogr. A 1218 (2011) 4406–4416, http://dx.doi.org/10.1016/j.chroma.2011.05.018.

[6] J.C. Heaton, X. Wang, W.E. Barber, S.M.C. Buckenmaier, D.V. McCalley, Practical observations on the performance of bare silica in hydrophilic interaction compared with C18 reversed-phase liquid chromatography, J. Chromatogr. A 1328 (2014) 7–15, http://dx.doi.org/10.1016/j.chroma.2013.12.058.

[7] M. Catani, O.H. Ismail, A. Cavazzini, A. Ciogli, C. Villani, L. Pasti, D.S. Bell, Rationale behind the optimum efficiency of columns packed with new 1.9µm fully porous particles of narrow particle size distribution, J. Chromatogr. A 1454 (2016) 78–85, http://doi:10.1016/j.chroma.2016.05.037.

[8] J.C. Heaton, D.V. McCalley, Comparison of the kinetic performance and retentivity of sub-2µm core–shell, hybrid and conventional bare silica phases in hydrophilic interaction chromatography, J. Chromatogr. A 1371 (2014) 106–116, http://doi:10.1016/j.chroma.2014.10.013.

[9] F. Gritti, K. Horvath, G. Guiochon, How changing the particle structure can speed up protein mass transfer kinetics in liquid chromatography, J. Chromatogr. A 1263 (2012) 84–98, http://doi:10.1016/j.chroma.2012.09.030.

[10] J.H. Knox , Band dispersion in chromatography –a new view of A -term dispersion, J. Chromatogr. A. 831 (1999) 3–15, http://doi.org/10.1016/S0021-9673(98)00497-X.

[11] F. Gritti, G. Guiochon, Comparison between the intra-particle diffusivity in the hydrophilic interaction chromatography and reversed phase liquid chromatography modes. Impact on the column efficiency. J. Chromatogr. A 1297 (2013) 85–95. http://doi:10.1016/j.chroma.2013.04.055.

[12] D. Cabooter, H. Song, D. Makey, D. Sadriaj, M. Dittmann, D. Stoll, G. Desmet, Measurement and modelling of the b-term and the intra-particle diffusion in reversed-phase liquid chromatography, J. Chromatogr. A 1637 (2021) 461852, http://doi.org/10.1016/j.chroma.2020.461852.

[13] H. Song, G. Desmet, D. Cabooter, Evaluation of the kinetic performance differences between hydrophilic-interaction liquid chromatography and reversed-phase liquid chromatography under conditions of identical packing structure, Anal. Chem. 87 (2015) 12331–12339, http://dx.doi.org/10.1021/acs.analchem.5b03697.

[14] N. Lambert, S. Miyazaki, M. Ohira, N. Tanaka, A. Felinger, Comparison of the kinetic performance of different columns for fast liquid chromatography, emphasizing the contributions of column end structure, J. Chromatogr. A 1473 (2016) 99-108, https://doi.org/10.1016/j.chroma.2016.10.052.

[15] F. Gritti, M. Dion, A. Felinger, M. Savaria, Characterization of radial and axial heterogeneities of chromatographic columns by flow reversal, J. Chromatogr. A 1567 (2018) 164–176, http://doi:10.1016/j.chroma.2018.07.011.

[16] A. Andres, K. Broeckhoven, G. Desmet, Methods for the experimental characterization and analysis of the efficiency and speed of chromatographic columns: A step-by-step tutorial, Analytica Chimica Acta 894 (2015) 20-34, https://doi.org/10.1016/j.aca.2015.08.030.

[17] F. Gritti, G. Guiochon, Accurate measurements of peak variances: importance of this accuracy in the determination of the true corrected plate heights of chromatographic columns, J. Chromatogr. A 1218 (2011) 4452–4461, http://dx.doi.org/10.1016/j.chroma.2011.05.035.

[18] Y. Vanderheyden, K. Broeckhoven, G. Desmet, Comparison and optimization of different peak integration methods to determine the variance of unretained and extra-column peaks, J. Chromatogr. A 1364 (2014) 140–150, http://doi.org/10.1016/j.chroma.2014.08.066.

[19] H. Song, D. Sadriaj, G. Desmet, D. Cabooter, Methodologies to determine b-term coefficients revisited, J. Chromatogr. A 1532 (2018) 124–135, https://doi.org/10.1016/j.chroma.2017.11.070.

[20] A. Felinger, Data Analysis and Signal Processing in Chromatography, Elsevier, Amsterdam, The Netherlands, 1998.

[21] Y. Vanderheyden, K. Broeckhoven, G. Desmet, Peak deconvolution to correctly assess the band broadening of chromatographic columns, J. Chromatogr. A 1465 (2016) 126–142, https://doi.org/10.1016/j.chroma.2016.08.058.

[22] F. Gritti, A stochastic view on column efficiency, J. Chromatogr. A. 1540 (2018) 55–67, http://doi.org/10.1016/j.chroma.2018.02.005.

[23] F. Gritti, On the relationship between radial structure heterogeneities and efficiency of chromatographic columns, J. Chromatogr. A 1533 (2018) 112–126, http://doi.org/10.1016/j.chroma.2017.12.030.

[24] A. Reising, S. Schlabach, V. Baranau, D. Stoeckel, U. Tallarek, Analysis of packing microstructure and wall effects in a narrow-bore ultrahigh pressure liquid chromatography column using focused ion beam scanning electron microscopy, J. Chromatogr. A 1513 (2017) 172–182, http://dx.doi.org/10.1016/j.chroma.2017.07.049.

[25] T.J.R. Hughes, The Finite Element Method: Linear Static and Dynamic Finite Element Analysis, Prentice-Hall, Hoboken, New Jersey, 1987.

[26] R. Aris, On the dispersion of a solute in a fluid flowing through a tube. Proc. R. Soc. A 235 (1956) 67–77, https://doi.org/10.1098/rspa.1956.0065.

[27] G. Desmet, A finite parallel zone model to interpret and extend Giddings' coupling theory for the eddy-dispersion in porous chromatographic media, J. Chromatogr. A 1314 (2013) 124–137, http://dx.doi.org/10.1016/j.chroma.2013.09.016.

[28] J.C. Giddings, Dynamics of Chromatography: Principles and Theory, M. Dekker, New York City, New York, 1965.

[29] O. Levenspiel, Chemical Reactor Engineering: an Introduction to the Design of Chemical Reactors, John Wiley and Sons, Hoboken, New Jersey, 1962.

[30] D. Zelenyánszki, N. Lambert, F. Gritti, A. Felinger, The effect of column packing procedure on column end efficiency and on bed heterogeneity – experiments with flow-reversal. J. Chromatogr. A 1603 (2019) 412-416, http://doi:10.1016/j.chroma.2019.05.040.

Figure captions

Figure 1. (a) Deconvoluted "parking-only peak" (solid line) as obtained under the experimental conditions described in the main text, as compared to the best Gaussian fit (dashed line). **(b)** Zoom-in of (a).

Figure 2. Velocity profiles considered in the present study: **(a)** the parabolic flow profile ($\Delta u/u = 0.04$) and **(b)** the side-wall flow profile ($\Delta u/u = 0.23$) (adapted from [23] and [24]).

Figure 3. Concentration profiles **(a-d)** and peak shapes **(e-h)** resulting from the parabolic flow profile: **(a,e)** at the beginning of peak parking, **(b,f)** at the end of peak parking, **(c,g)** as the peak exits the column and **(d,h)** idem as (c,g), but in the absence of peak parking. ($\Delta u/u = 0.04$)

Figure 4. Concentration profiles **(a-d)** and peak shapes **(e-h)** resulting from the side-wall flow profile: **(a,e)** at the beginning of peak parking, **(b,f)** at the end of peak parking, **(c,g)** as the peak exits the column and **(d,h)** idem as (c,g), but in the absence of peak parking. ($\Delta u/u = 0.23$)

Figure 5. Evolution of the peak's variance **(a,d)** and skewness **(c,f)** as a function of time. Panel **(b)** shows a zoom of panel (a). Panel **(e)** shows a schematic of the AB-, BC- and AC-trajectories in simulations with (top) and without peak parking (bottom).

Figure 6. Deconvolution of the peak shapes with and without peak parking (black), as compared to the deconvolution of the peak shapes before and after peak parking (gray).

Figure 7. Deconvolution of the peak shapes with and without peak parking **(a,c)** for various values of the relative velocity difference (parabolic: $\Delta u/u = 0.02$ (blue), $\Delta u/u = 0.04$ (black), $\Delta u/u = 0.08$ (red); realistic: $\Delta u/u = 0.12$ (blue), $\Delta u/u = 0.23$ (black), $\Delta u/u = 0.47$ (red)) and **(b,d)** for various values of the peak parking time ($t_{PP} = 10\ min$ (red), $t_{PP} = 40\ min$ (black), $t_{PP} = 80\ min$ (blue)).

Figure 8. Error on the band broadening caused by peak parking **(a,c)** as a function of the relative velocity difference and **(b,d)** as a function of the peak parking time. The simulation data (dots) are fitted (line) with a quadratic equation in panels (a) and (c), and with three terms of Eq. (20) in panels (b) ($\alpha_1 = 0.48\ mm^2$, $\alpha_2 = 0.01\ mm^2$ and $\alpha_3 = 0.01\ mm^2$) and (d) ($\alpha_1 = 0.26\ mm^2$, $\alpha_2 = 0.04\ mm^2$ and $\alpha_3 = 0.20\ mm^2$).

Figure 9. (a,c) Deconvolution of the peak shapes with and without peak parking, simulating different experimental set-ups: parking at the midpoint of the column, parking at either 1/6 or 5/6 of the column's length (red) and parking with flow reversal (blue). **(b,d)** Deconvolution of the peak shapes

using different peak parking times: deconvoluting $t_{PP} = 80\ min$ with respect to $t_{PP} = 0\ min$ (black) and deconvoluting $t_{PP} = 160\ min$ with respect to $t_{PP} = 80\ min$ (green).

Figure 1

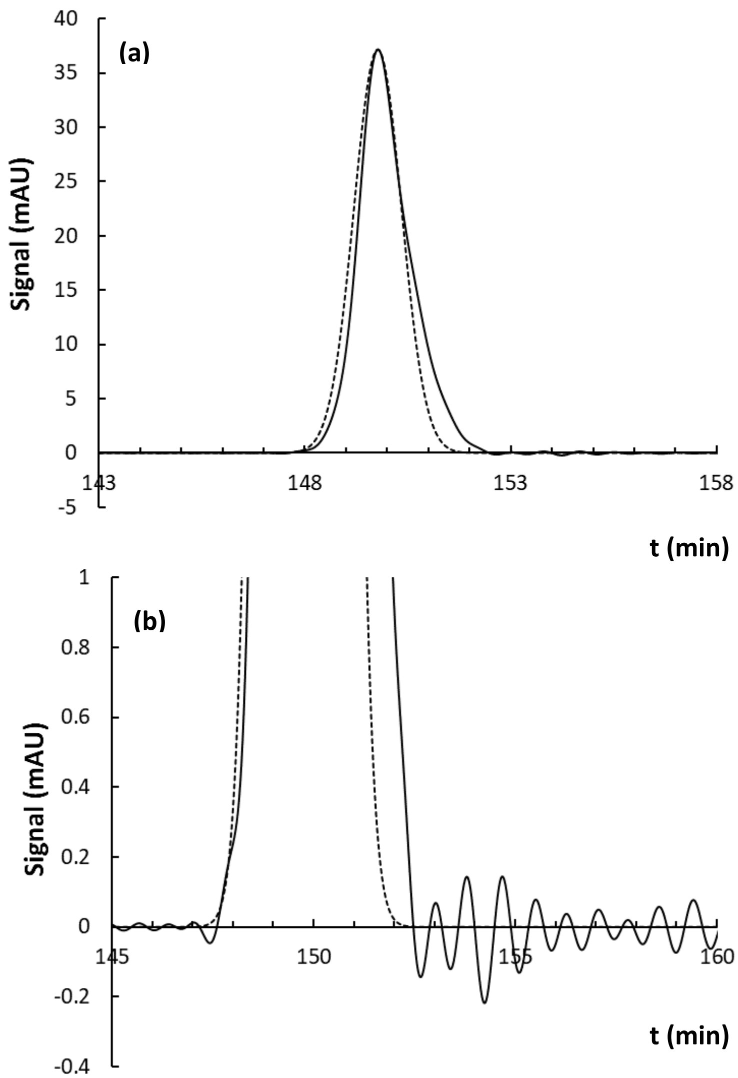

(a)
Signal (mAU)
40
35
30
25
20
15
10
5
0
-5
143
148
153
158
t (min)
(b)
Signal (mAU)
1
0.8
0.6
0.4
0.2
0
-0.2
-0.4
145
150
155
160
t (min)

Figure 2

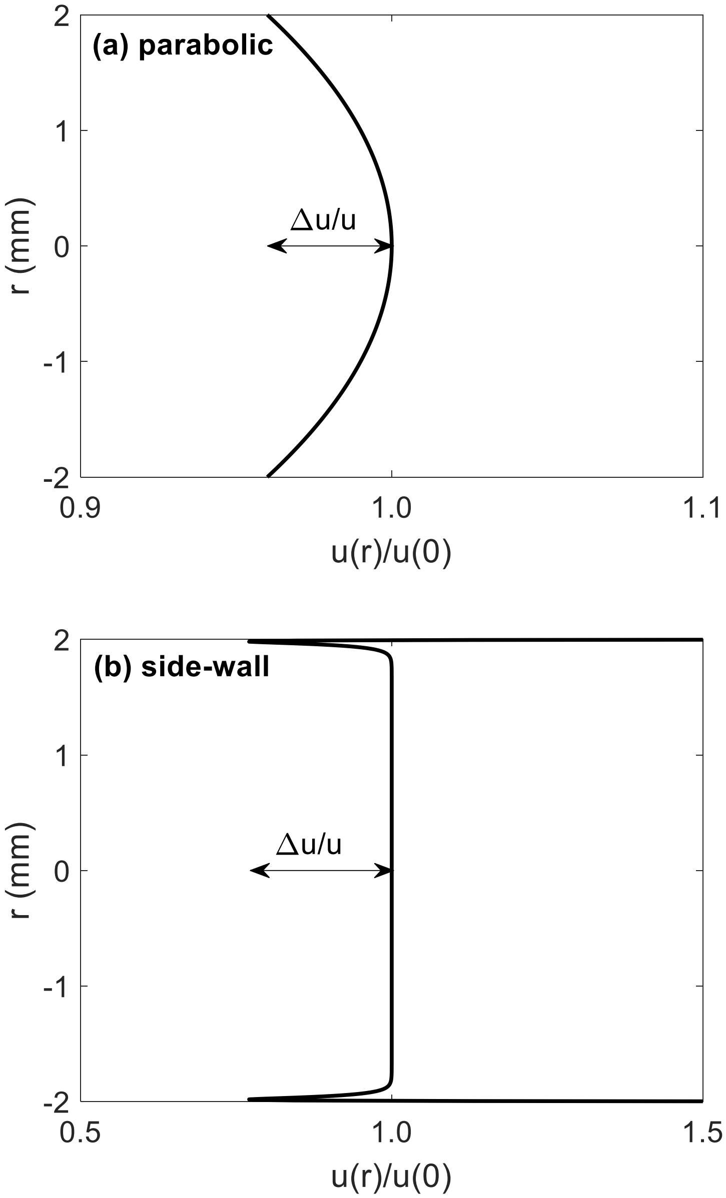

(a) parabolic
Δu/u
r (mm)
u(r)/u(0)
2
1
0
-1
-2
0.9
1.0
1.1
(b) side-wall
Δu/u
r (mm)
u(r)/u(0)
2
1
0
-1
-2
0.5
1.0
1.5

Figure 3

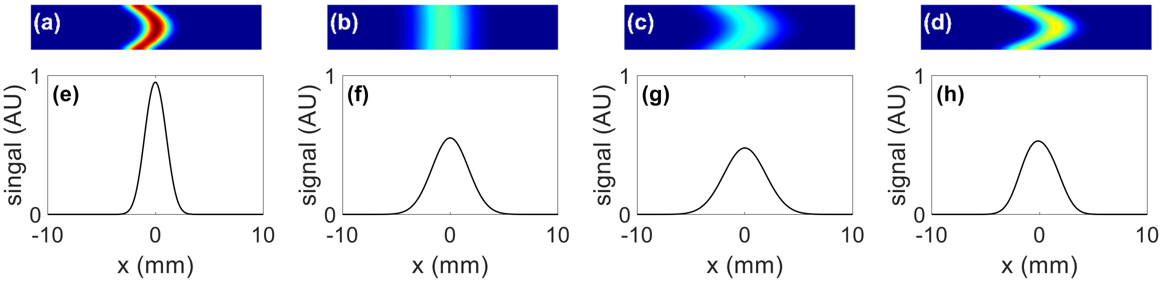

Figure 4

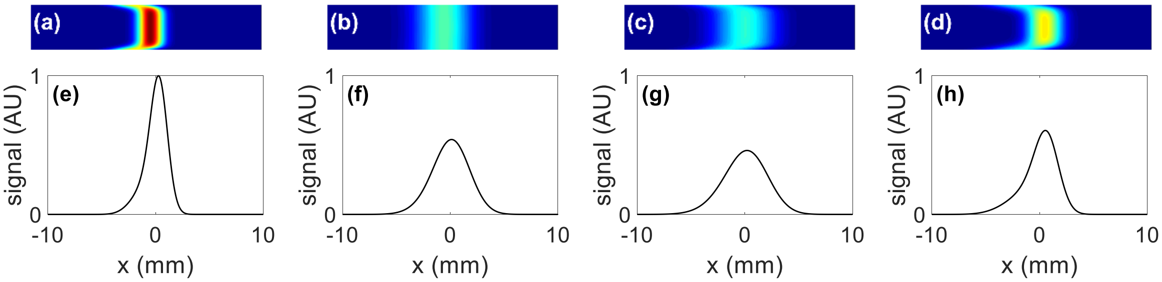

Figure 5

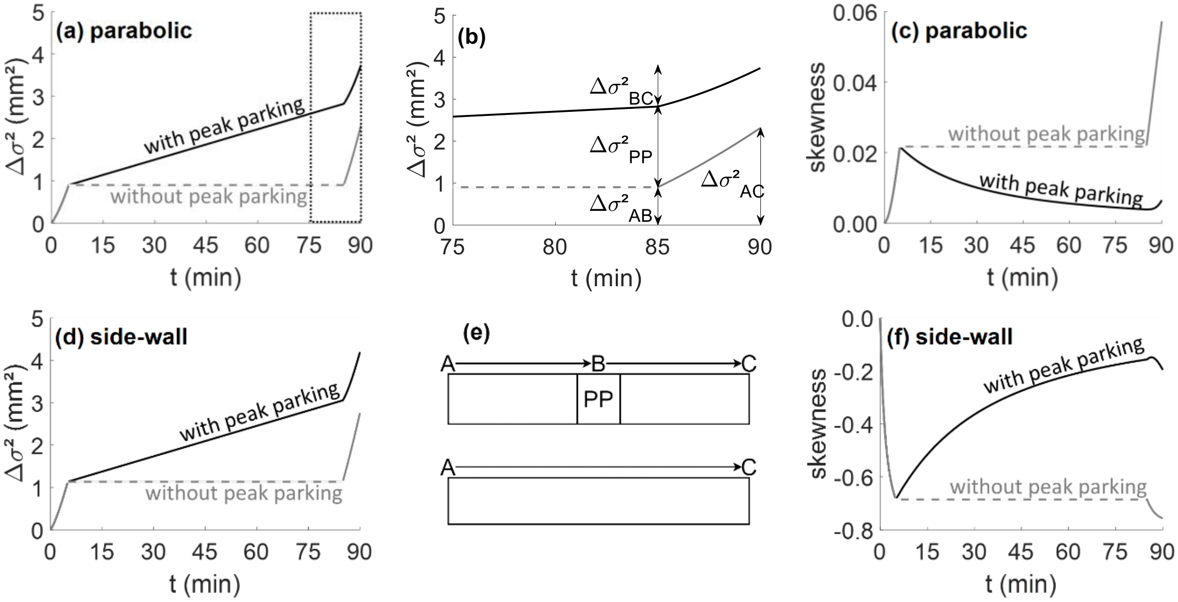
(a) parabolic
with peak parking
without peak parking
$\Delta\sigma^2$ (mm²)
t (min)
(b)
$\Delta\sigma^2_{BC}$
$\Delta\sigma^2_{PP}$
$\Delta\sigma^2_{AB}$
$\Delta\sigma^2_{AC}$
$\Delta\sigma^2$ (mm²)
t (min)
(c) parabolic
without peak parking
with peak parking
skewness
t (min)
(d) side-wall
with peak parking
without peak parking
$\Delta\sigma^2$ (mm²)
t (min)
(e)
A
B
C
PP
A
C
(f) side-wall
with peak parking
without peak parking
skewness
t (min)

Figure 6

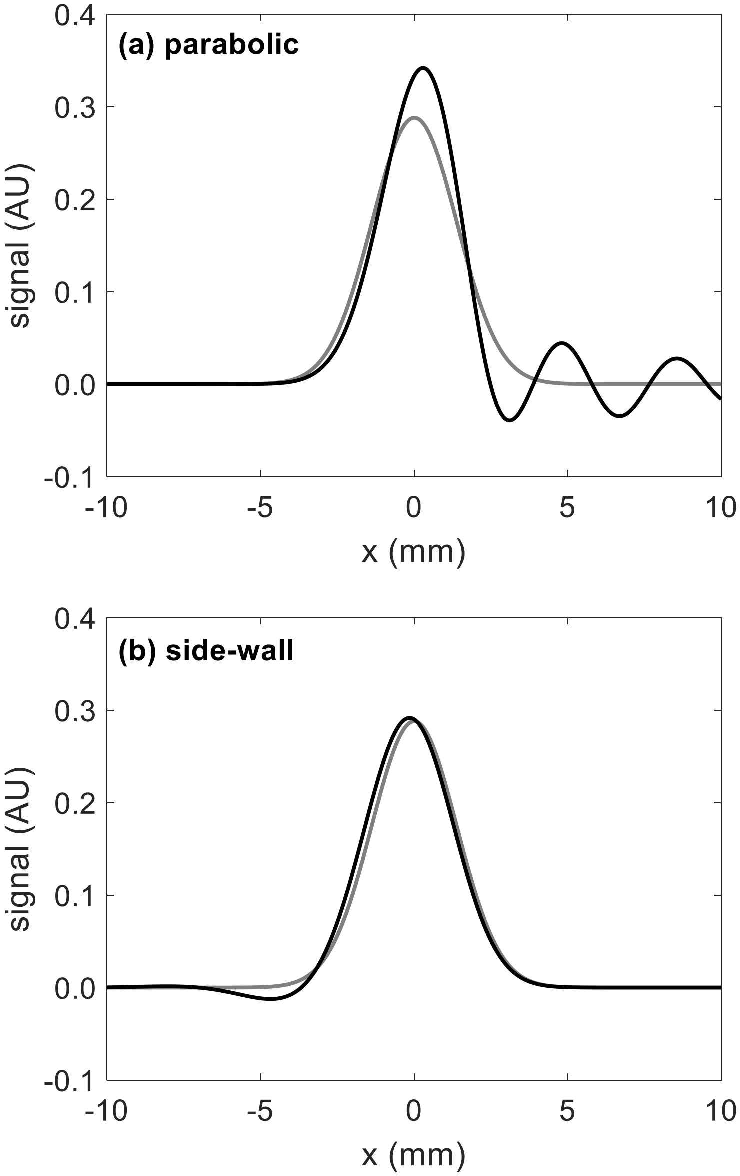

(a) parabolic
signal (AU)
x (mm)
0.4
0.3
0.2
0.1
0.0
-0.1
-10
-5
0
5
10
(b) side-wall
signal (AU)
x (mm)
0.4
0.3
0.2
0.1
0.0
-0.1
-10
-5
0
5
10

Figure 7

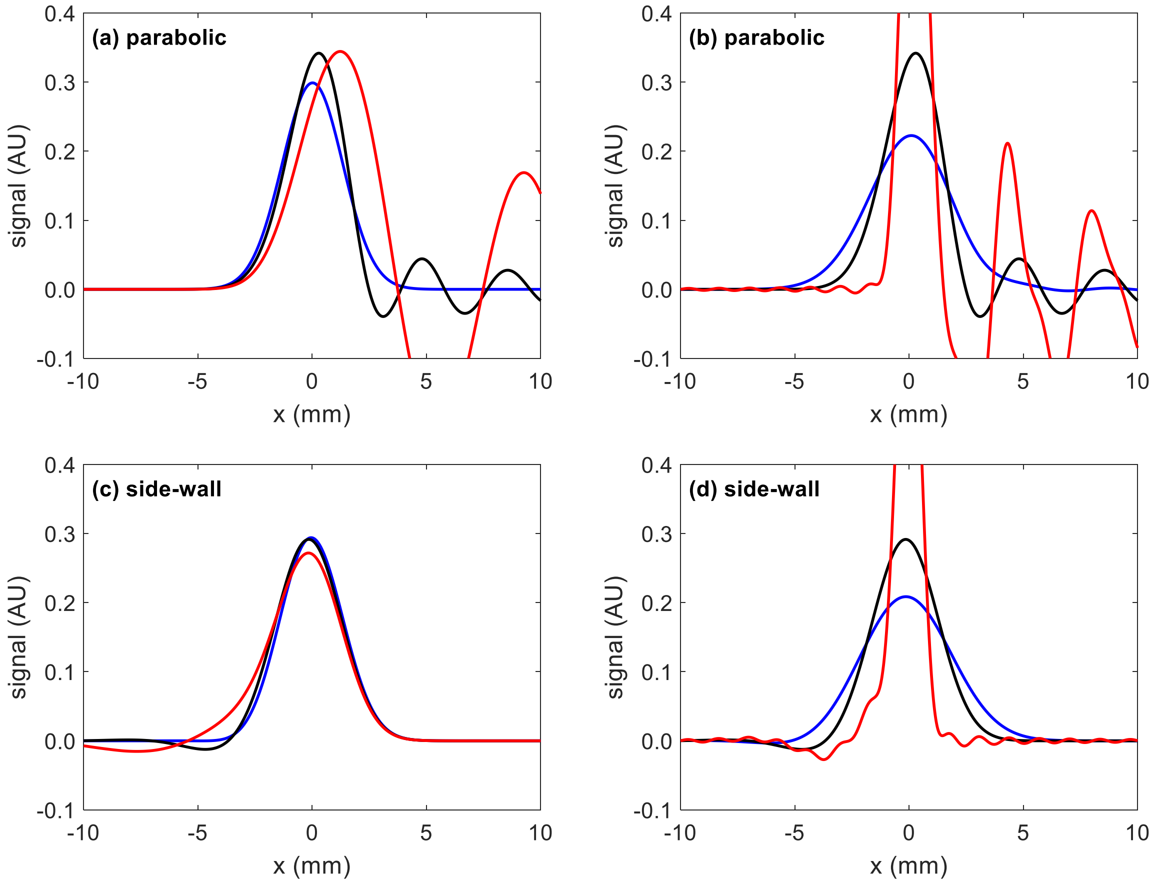
(a) parabolic
(b) parabolic
(c) side-wall
(d) side-wall
signal (AU)
x (mm)
0.4
0.3
0.2
0.1
0.0
-0.1
-10
-5
0
5
10

Figure 8

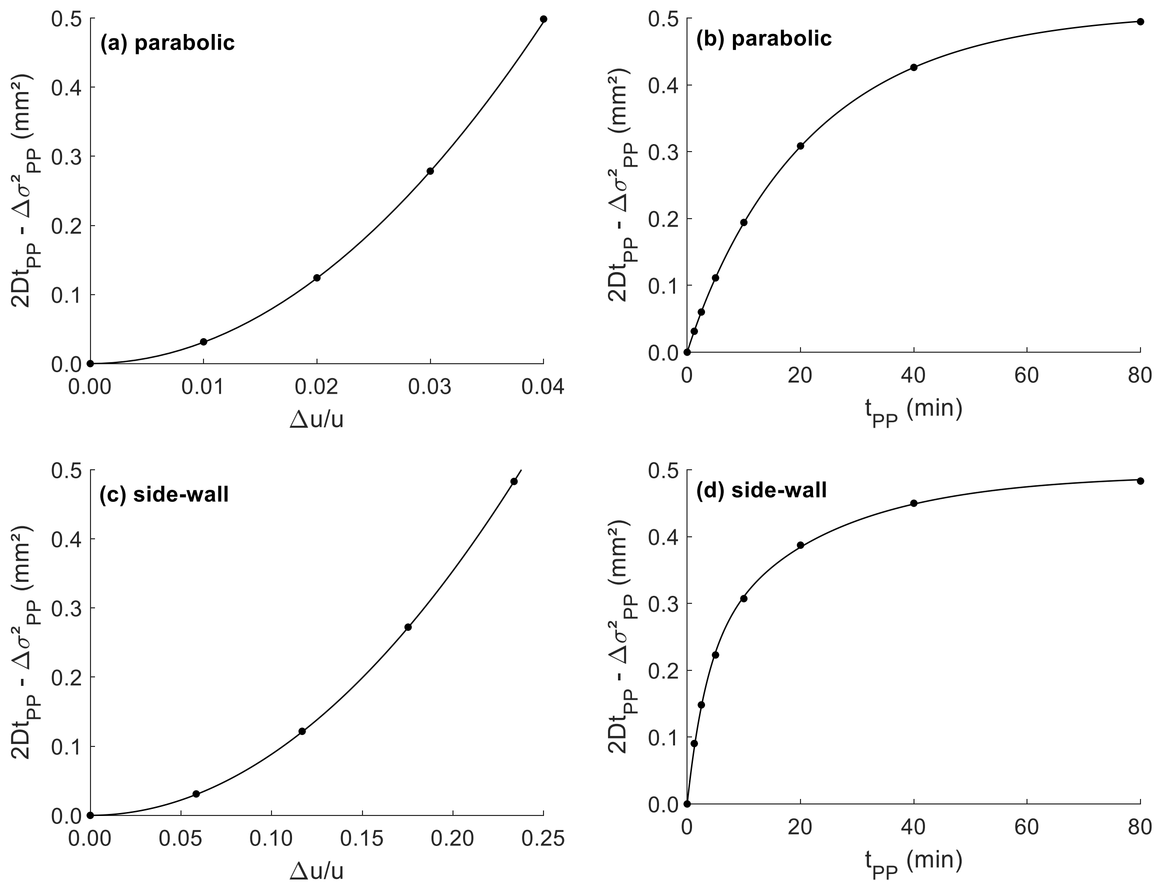
(a) parabolic
(b) parabolic
(c) side-wall
(d) side-wall
$2Dt_{PP} - \Delta\sigma^2_{PP}$ (mm²)
$\Delta u/u$
t_{PP} (min)
0.0
0.1
0.2
0.3
0.4
0.5
0.00
0.01
0.02
0.03
0.04
0.05
0.10
0.15
0.20
0.25
0
20
40
60
80

Figure 9

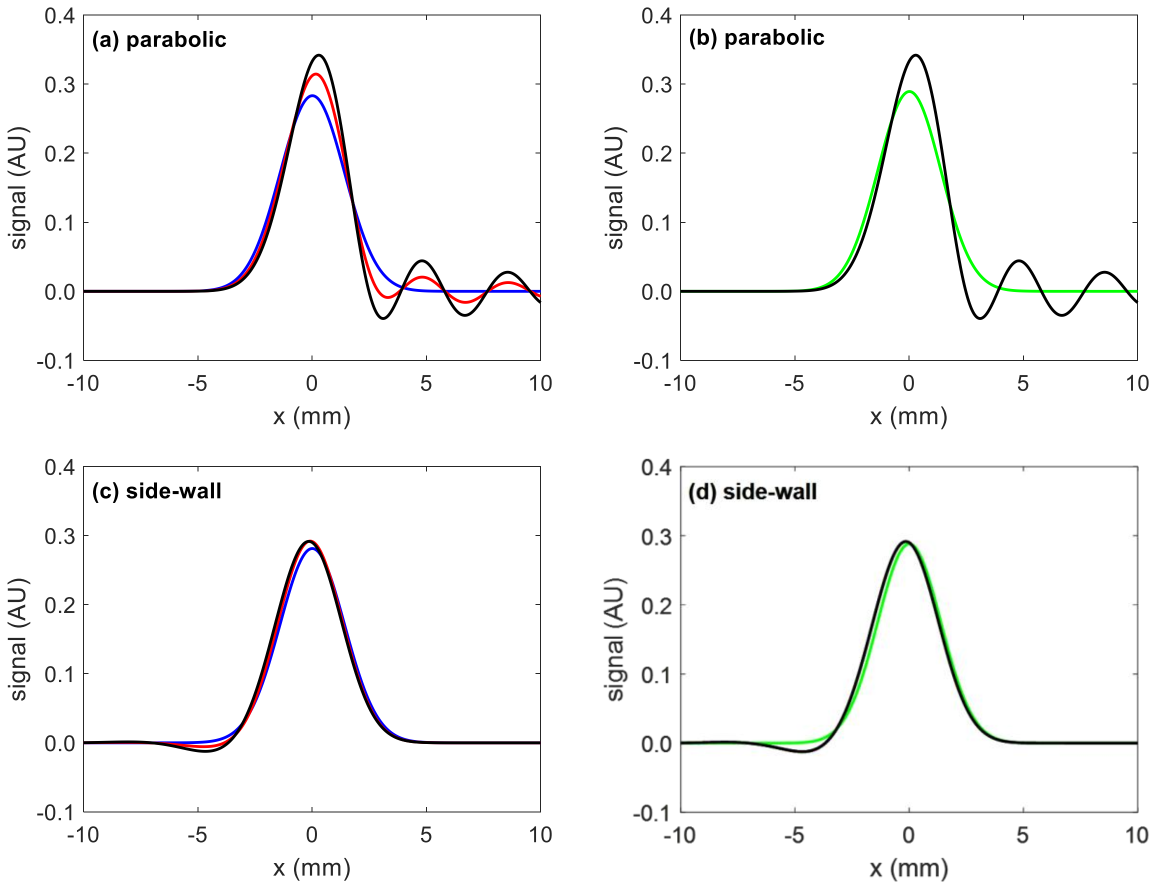
(a) parabolic
(b) parabolic
(c) side-wall
(d) side-wall
signal (AU)
x (mm)
0.4
0.3
0.2
0.1
0.0
-0.1
-10
-5
0
5
10

Table 1. Parameters of the peak parking simulations.

parameter	symbol	value
column diameter	d_c	$4\ mm$
column length	L_c	$100\ mm$
dispersion coefficient (axial)	D_{ax}	$1e-9\ m^2/s$
dispersion coefficient (radial)	D_{rad}	$2e-10\ m^2/s$
effective diffusion coefficient	D_{eff}	$2e-10\ m^2/s$
particle diameter	d_p	$5\ \mu m$
peak parking time	t_{PP}	$80\ min$
relative velocity difference	ω, ω_{TLOPL} and ω_{WDRPL}	0.04, 1.50 and 0.50
retention factor	k	5
unretained velocity	u_0	$1\ mm/s$

Supplementary Material for:

Detailed numerical analysis of the effect of radial column heterogeneities on peak parking experiments with slowly diffusing analytes

Bram Huygens[(1)], Huiying Song[(2,3)], Deirdre Cabooter[(2)], Gert Desmet[(1,*)]

[(1)] Vrije Universiteit Brussel, Department of Chemical Engineering, Pleinlaan 2, 1050 Brussel, Belgium

[(2)] KU Leuven, Department for Pharmaceutical and Pharmacological Sciences, Pharmaceutical Analysis, Herestraat 49, Leuven, Belgium

[(3)] current affiliation: Janssen Pharmaceutica, Process Analytical Research, Chemical Process Research & Development, Turnhoutseweg 30, Beerse, Belgium

(*) corresponding author: tel.: (+) 32 (0)16.32.34.42, fax: (+) 32 (0)16.32.34.48, e-mail: gedesmet@vub.be

Abstract

In this Supplementary Material, we provide figures to support the discussion in the main text.

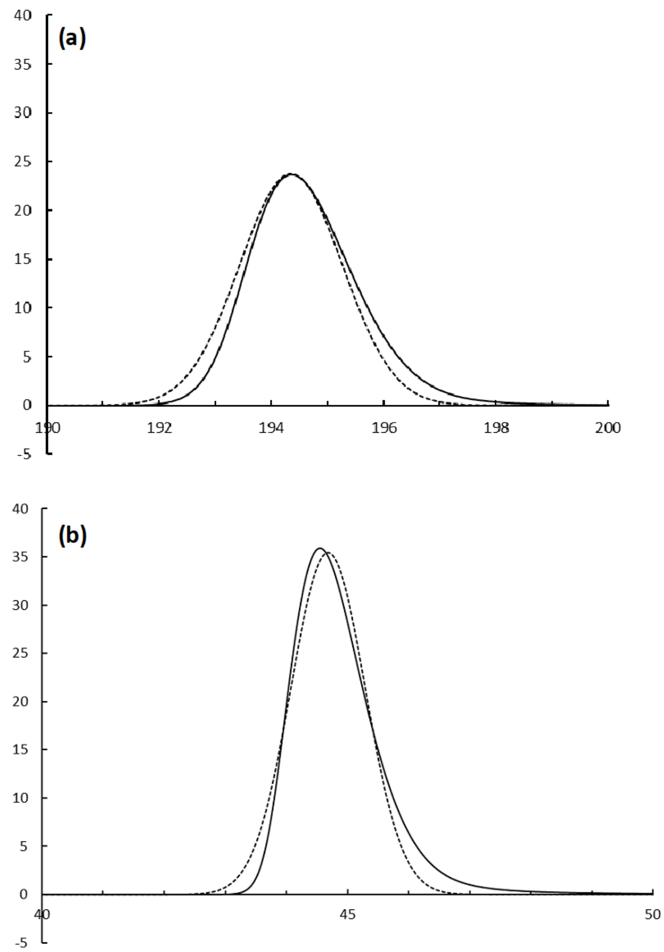

Figure S-1. (a) Peak recorded after 150min peak parking experiment recorded under the conditions described in the experimental section **(b)** “no parking” peak (=peak recorded after a 1min parking time) used for the deconvolution of the 150min parking peak leading to the deconvoluted “parking-only” peak shown in Fig. 1 of the main text. Dashed curves are the best fitting Gaussian curves added as a reference.

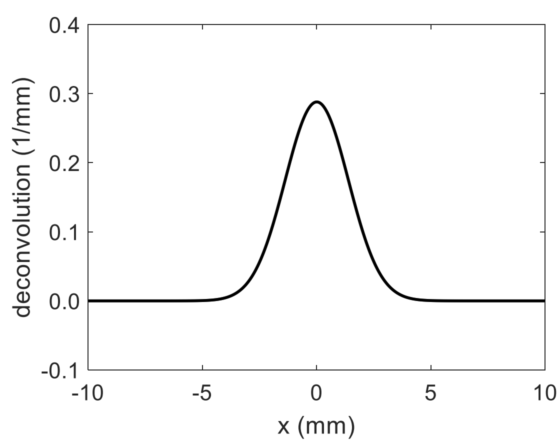

Figure S-2. Deconvolution of the peak shapes with and without peak parking (cf. Fig. 6) in the case of plug flow, resulting in a Gaussian peak shape.

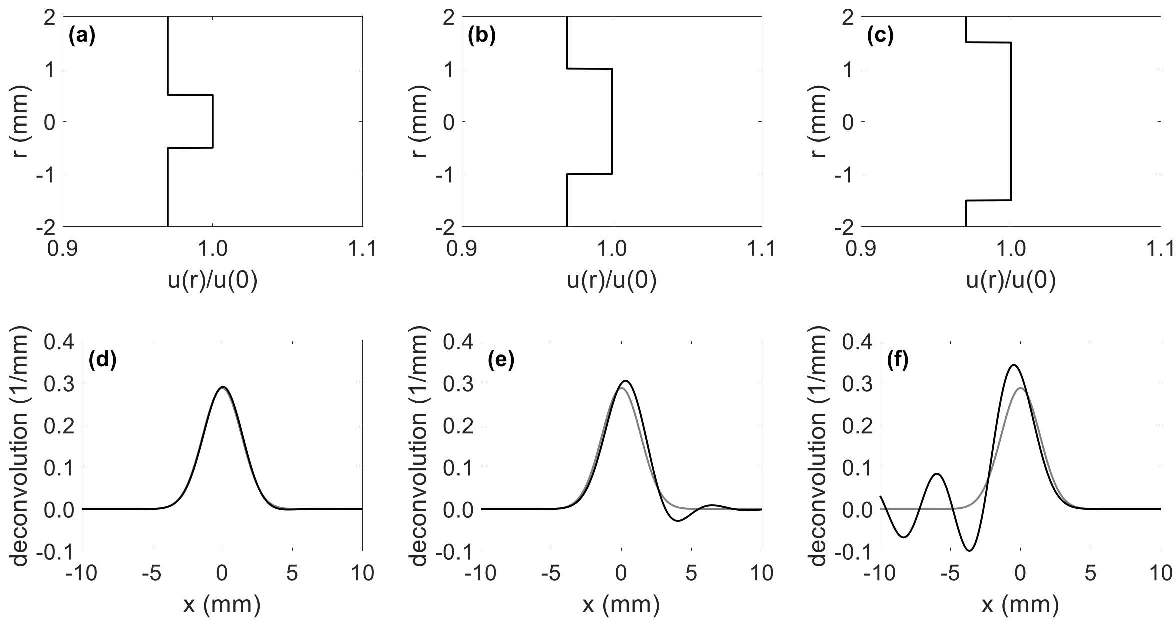

Figure S-3. Deconvolution of the peak shapes with and without peak parking (black), as compared to the deconvolution of the peak shapes before and after peak parking (gray) (cf. Fig. 6). Three cases are shown, each of them having a stepwise flow profile ($\Delta u/u = 0.03$).

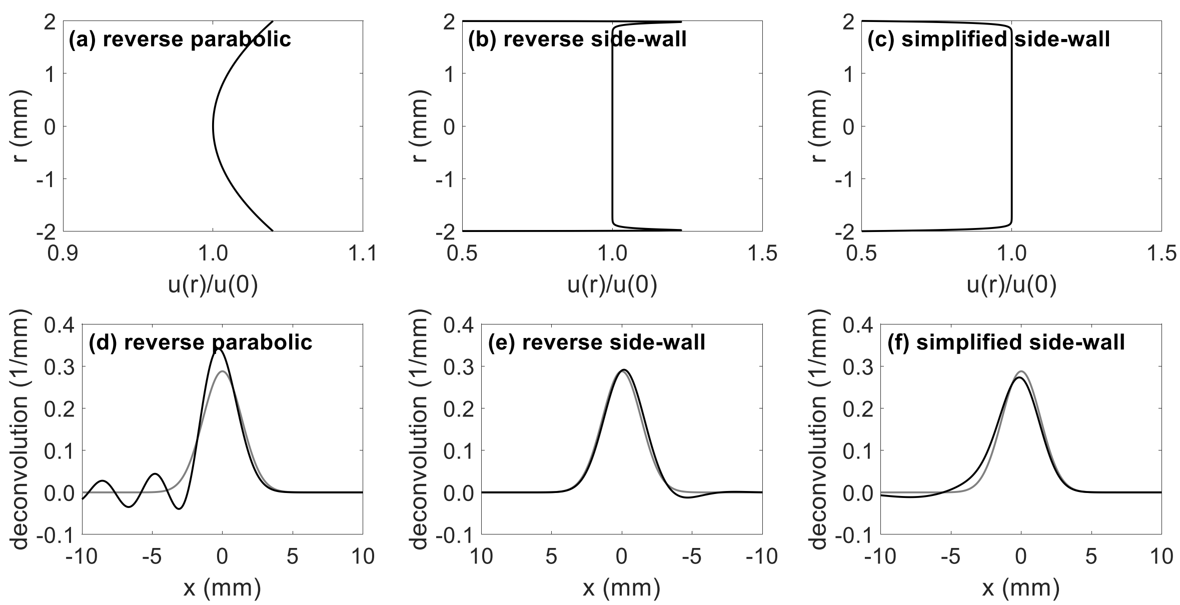

Figure S-4. Deconvolution of the peak shapes with and without peak parking (black), as compared to the deconvolution of the peak shapes before and after peak parking (gray) (cf. Fig. 6). Three cases are shown: the ‘reverse’ flow profiles are obtained by changing the sign of the velocity difference, the ‘simplified’ flow profile is obtained by having $\omega_{TLOPL} = 0$ in Eq. (4).

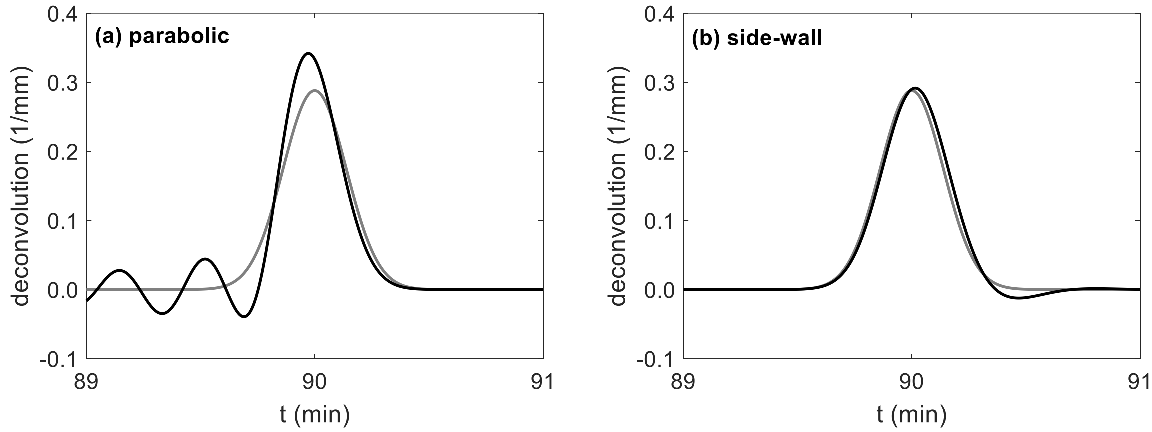

Figure S-5. Variant of Fig. 6 in the main text, plotted in the time domain.

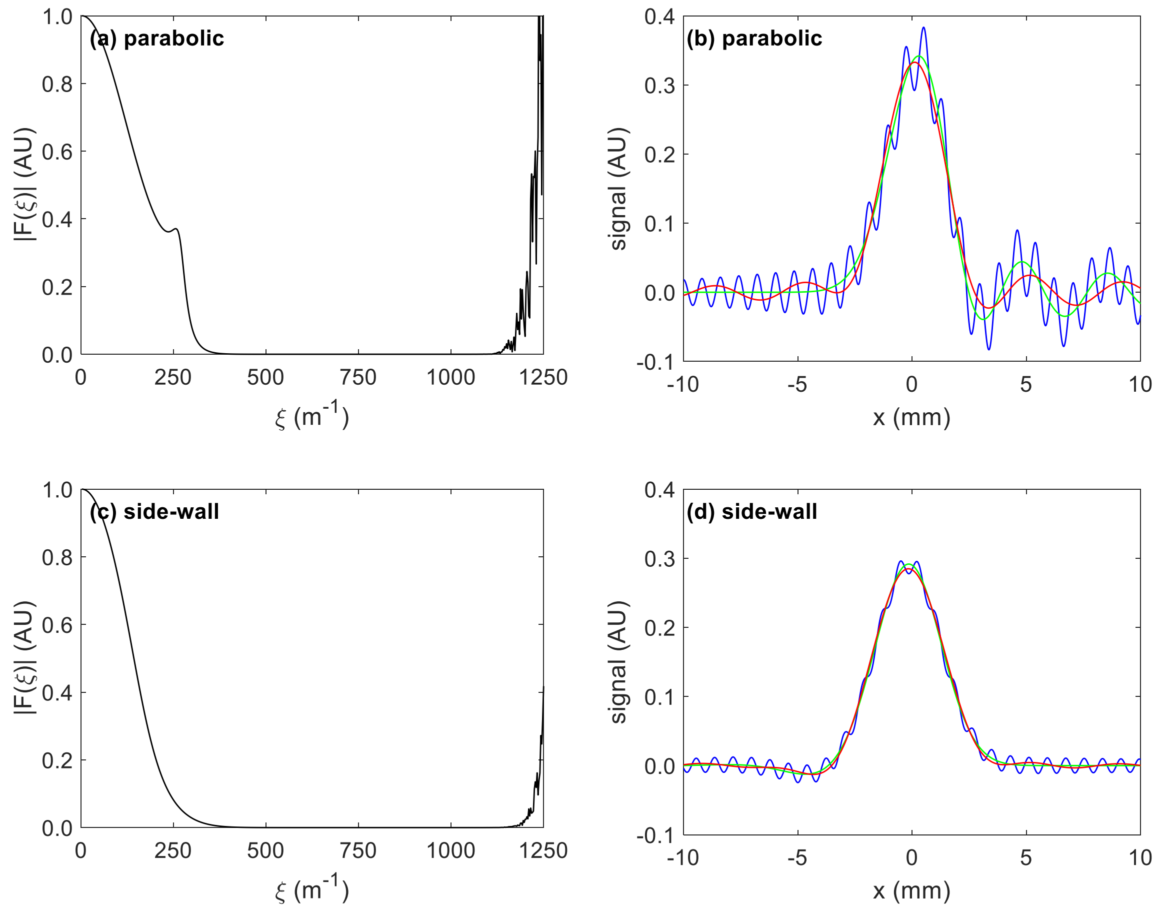

Figure S-6. (a,c) Division of the Fourier spectra with and without peak parking (cf. division in Eq. (10)). **(b,d)** Deconvolutions computed based on different cut-off wavenumbers. Red: low cut-off ($\xi_{CO} = 250\,m^{-1}$), resulting in Gibbs phenomenon. Green: suitable cut-off ($\xi_{CO} = 750\,m^{-1}$), as shown in e.g. Fig. 6. Blue: high cut-off ($\xi_{CO} = 1250\,m^{-1}$), resulting in spurious oscillations. Note that any cut-off wavenumber between $500\,m^{-1}$ and $1000\,m^{-1}$ is suitable, resulting in a deconvolution similar to the green curve.